Monthly Notices
of the
ROYAL ASTRONOMICAL SOCIETY

MNRAS **446,** 2823–2836 (2015) doi:10.1093/mnras/stu2256

Differences between CO- and calcium triplet-derived velocity dispersions in spiral galaxies: evidence for central star formation?

Rogemar A. Riffel,[1⋆] Luis C. Ho,[2,3] Rachel Mason,[4] Alberto Rodríguez-Ardila,[5] Lucimara Martins,[6] Rogério Riffel,[7] Ruben Diaz,[8] Luis Colina,[9] Almudena Alonso-Herrero,[10] Helene Flohic,[11] Omaira Gonzalez Martin,[12,13,14] Paulina Lira,[15] Richard McDermid,[4,16] Cristina Ramos Almeida,[12,13] Ricardo Schiavon,[2,17] Karun Thanjavur,[18] Daniel Ruschel-Dutra,[7,12] Claudia Winge[8] and Eric Perlman[19]

Affiliations are listed at the end of the paper

Accepted 2014 October 24. Received 2014 October 24; in original form 2014 May 20

ABSTRACT

We examine the stellar velocity dispersions (σ) of a sample of 48 galaxies, 35 of which are spirals, from the Palomar nearby galaxy survey. It is known that for ultra-luminous infrared galaxies (ULIRGs) and merger remnants, the σ derived from the near-infrared CO band heads is smaller than that measured from optical lines, while no discrepancy between these measurements is found for early-type galaxies. No such studies are available for spiral galaxies – the subject of this paper. We used cross-dispersed spectroscopic data obtained with the Gemini Near-Infrared Spectrograph, with spectral coverage from 0.85 to 2.5 μm, to obtain σ measurements from the 2.29 μm CO band heads ($\sigma_{\rm CO}$) and the 0.85 μm calcium triplet ($\sigma_{\rm CaT}$). For the spiral galaxies in the sample, we found that $\sigma_{\rm CO}$ is smaller than $\sigma_{\rm CaT}$, with a mean fractional difference of 14.3 per cent. The best fit to the data is given by $\sigma_{\rm opt} = (46.0 \pm 18.1) + (0.85 \pm 0.12)\sigma_{\rm CO}$. This '$\sigma$-discrepancy' may be related to the presence of warm dust, as suggested by a slight correlation between the discrepancy and the infrared luminosity. This is consistent with studies that have found no σ-discrepancy in dust-poor early-type galaxies, and a much larger discrepancy in dusty merger remnants and ULIRGs. That $\sigma_{\rm CO}$ is lower than $\sigma_{\rm opt}$ may also indicate the presence of a dynamically cold stellar population component. This would agree with the spatial correspondence between low-$\sigma_{\rm CO}$ and young/intermediate-age stellar populations that has been observed in spatially resolved spectroscopy of a handful of galaxies.

Key words: galaxies: active – galaxies: kinematics and dynamics – galaxies: star formation – infrared: galaxies.

1 INTRODUCTION

The empirical relationship between the stellar velocity dispersion (σ) of the spheroidal component of galaxies and the mass of the supermassive black hole (SMBH; $M_\bullet$) at their centre (e.g. Ferrarese & Merrit 2000; Gebhardt et al. 2000) has been extensively used to estimate $M_\bullet$ in active and inactive galaxies. More direct determinations of $M_\bullet$, through stellar kinematics within the black hole's sphere of influence, or broad emission line measurements, are only feasible for a limited number of objects, making the $M_\bullet$–σ relation a very useful alternative. Cosmological simulations suggest that the central SMBH evolves together with the host galaxy and plays a fundamental role in its evolution (Di Matteo, Springel & Hernquist 2005; Springel, Di Matteo & Hernquist 2005; Bower et al. 2006; Nemmen et al. 2007), and this co-evolution may be the mechanism that leads to the $M_\bullet$–σ relation. The intrinsic scatter in the relation (i.e. the range of $M_\bullet$ found for a given σ) therefore contains information about the processes of galaxy and black hole evolution (e.g. Gültekin et al. 2009). Besides the $M_\bullet$–σ relation, stellar velocity dispersion measurements are also relevant for many other astrophysical applications, including the galaxy Fundamental Plane (e.g. Djorgovski & Davis 1987; Dressler et al. 1987; Falcón-Barroso, Peletier & Balcells 2002; Bernardi et al. 2003; Gebhardt

⋆E-mail: rogemar@ufsm.br

et al. 2003; Valluri, Merrit & Emsellem 2004), the metallicity–σ relation (e.g. Terlevich et al. 1981; Dressler 1984a; Bender, Burstein & Faber 1993), the V/σ ratio that is an important criterion to determine the dynamical state of early-type galaxies (e.g. Cox et al. 2006; Cappellari et al. 2007; Naab et al. 2013), etc. For all of these reasons, understanding the factors affecting σ measurements is an important issue.

Measurements of σ in galaxies have traditionally been done at wavelengths <1 μm, often using the 'Mg*b*' line at 0.52 μm, or the 0.85 μm calcium triplet absorption (e.g. Ho et al. 2009). Measurements based on stellar absorption lines in the infrared (IR), on the other hand, can also probe regions that are obscured by dust at optical wavelengths, or different stellar populations from those revealed in the optical. For these reasons, several recent studies have compared σ values obtained from the fitting of stellar absorptions in the optical and in the near-IR (NIR) spectral regions, generally using the CO absorption band heads in the *H* and *K* bands (Silge & Gebhardt 2003; Rothberg & Fischer 2010; Vanderbeke et al. 2011; Kang et al. 2013; Rothberg et al. 2013).

Silge & Gebhardt (2003) presented stellar velocity dispersions measured from the 2.29 μm CO band head in a sample composed of 18 lenticular (S0) and 7 elliptical galaxies. The resulting sigma values were compared with the literature values derived primarily from fitting the Ca II lines near 4000 Å, the Mg*b* lines near 5175 Å, and the 8500 Å Ca II triplet (hereafter CaT). The $\sigma_{\rm CO}$ values were found to be up to 30 per cent smaller than $\sigma_{\rm opt}$, with a median difference of 11 per cent[1]. However, this difference was observed only in the lenticular galaxies; in the elliptical galaxies, the optical and IR measurements were consistent. The authors speculate that the difference may be related to the presence and distribution of dust in the S0 objects: if the dust is mainly located in the stellar disc, optical σ measurements will be biased towards the less obscured, dynamically hotter bulge component <1 μm.

Vanderbeke et al. (2011) measured $\sigma_{\rm CO}$ in a sample of 19 Fornax cluster members, composed of roughly equal numbers of elliptical and lenticular galaxies. These measurements were compared with $\sigma_{\rm opt}$ from Kuntschner (2000) and found to be consistent, with $\sigma_{\rm frac} = \frac{\sigma_{\rm CO}-\sigma_{\rm opt}}{\sigma_{\rm opt}} = 6.4$ per cent. The lack of a discernible difference between $\sigma_{\rm CO}$ and $\sigma_{\rm opt}$ in the lenticular galaxies does not agree with the findings of Silge & Gebhardt (2003). It is, however, consistent with a previous study of velocity dispersions in the Fornax cluster by Silva, Kuntschner & Lyubenova (2008).

Optical and IR velocity dispersions were also compared by Kang et al. (2013). This work used the CO absorption bands around 1.6 μm, rather than those near 2.3 μm, to derive $\sigma_{\rm CO}$ for 31 galaxies: 19 ellipticals, 9 lenticulars, and 3 spirals. No significant difference was found between $\sigma_{\rm CO}$ and $\sigma_{\rm opt}$ (based mainly on the CaT). This suggests that both sets of lines probe roughly the same stars, and provides no evidence for a dynamically cold, obscured population.

Rothberg & Fischer (2010) also compared $\sigma_{\rm CO}$ and $\sigma_{\rm CaT}$ for a set of galaxies. This time, however, they studied 14 galaxy mergers, accompanied by a control sample of 23 elliptical galaxies. The measurements for the control sample were taken mostly from the literature, and $\sigma_{\rm CO}$ and $\sigma_{\rm CaT}$ were found to be similar, in agreement with the studies above. On the other hand, large differences are found for the mergers. In particular, for luminous infrared galaxies (LIRGs; six objects in their sample), the σ derived in the optical is up to twice the value obtained for the NIR. For the remaining eight non-LIRG mergers, $\sigma_{\rm CaT}$ is slightly larger than $\sigma_{\rm CO}$. Even larger discrepancies have been found for single nucleus ultra-luminous infrared galaxies (ULIRGs), for which $\sigma_{\rm CaT}$ can be three times larger than $\sigma_{\rm CO}$ (Rothberg et al. 2013). The discrepancies arise because $\sigma_{\rm CO}$, although conveniently insensitive to dust absorption, probes a luminous, young stellar disc, whereas $\sigma_{\rm CaT}$ gives information about an older stellar population that is more representative of the galaxy's overall dynamical mass. CO-based σ measurements imply that ULIRGs cannot be the progenitors of giant elliptical galaxies, whereas CaT-based values are consistent with a range of final galaxy masses.

The above studies have compared optical and CO-based σ measurements for early-type (E and S0) galaxies, and for galaxy mergers and ULIRGs. Little information is available, though, for late-type (spiral) objects, so the range of morphological types in which the large differences between $\sigma_{\rm CO}$ and $\sigma_{\rm CaT}$ occur is not yet known. We aim to rectify this situation by measuring $\sigma_{\rm CO}$ and $\sigma_{\rm CaT}$ in a sample of 48 nearby galaxies: 35 spirals, 7 lenticulars, and 6 ellipticals. We do this using slit spectroscopy covering simultaneously the CaT and 2.29 μm CO spectral regions. In Section 2, we describe the sample and the observational data, and in Section 3, we discuss the methods used to measure the stellar dispersion in the optical and in the NIR. The results are presented in Section 4, while their implications are discussed in Section 5. The conclusions of the present paper are given in Section 6.

2 OBSERVATIONS AND DATA REDUCTION

The sample of galaxies used in this work comprises 48 objects selected from the Palomar spectroscopic survey of nearby galaxies (Ho, Filippenko & Sargent 1995, 1997), covering a wide range of luminosity and nuclear activity type. Some properties of the sample are shown in Table 1, while full details of the overall programme, sample, observations, and data reduction are given in Mason et al. (submitted).

Briefly, the spectroscopic data were obtained in queue mode[2] with the Gemini Near-Infrared Spectrograph (GNIRS) on the Gemini North telescope. The cross-dispersed mode was used with the 32 l mm^{-1} grating, providing simultaneous spectral coverage from approximately 0.85 to 2.5 μm. We used the 0.3 arcsec × 7 arcsec slit, generally oriented along the mean parallactic angle at the time of the observations to minimize differential refraction effects. The data were obtained between 2011 October and 2013 May. Due to work done to address an issue with the 32 l mm^{-1} grating mount in 2012, the spectral resolution of the spectra obtained with the 0.3 arcsec slit after 2012 November differs from that achieved previously. The spectral resolution before 2012 November is 11.6 and 4.4 Å for the *K* band CO band heads and the CaT regions, respectively, obtained from the full width at half-maximum (FWHM) of the arc lamp calibration spectra. These values correspond to a resolution in velocity dispersion of ∼65 km s^{-1} for both regions. After 2012 November, the resulting spectral resolutions are 18.2 and 7.4 Å corresponding to ∼100 and ∼110 km s^{-1}.

The data were reduced using standard procedures.[3] To summarize, the raw frames are first cleaned of any electronic striping and

[1] We use $\sigma_{\rm CO}$ to denote velocity dispersions derived from the 2.29 μm CO bands, $\sigma_{\rm CaT}$ for those based on the CaT lines, and $\sigma_{\rm opt}$ as a general term to include all measurements based on lines at λ.

[2] Programmes GN-2011B-Q-111, GN-2012A-Q-23, GN-2012B-Q-80, GN-2012B-Q-112, GN-2013A-Q-16.

[3] Described at www.gemini.edu/sciops/instruments/gnirs/data-format-and-reduction/reducing-xd-spectra.

Table 1. Properties of the galaxies from our sample. Column 1: name of the object; column 2: morphological type from Ho et al. (1997); column 3: nuclear Activity from Ho et al. (1997) – S: Seyfert nucleus, L: LINER, T: transition object, and H: H II nucleus. ':' means that the classification is uncertain. Columns 4–9: stellar kinematic parameters. Column 10: the instrumental configuration used for the observations. Configuration 'a' corresponds to observations done before 2012 November and has an instrumental σ of 65 km s^{-1} for both spectral regions. Configuration 'b' corresponds to observations done after 2012 November and has an instrumental σ of 100 and 110 km s^{-1} for the CO and CaT regions. The uncertainties included for the kinematic parameters are those that PPXF outputs. The dashes in the table are due to the fact that for a few objects, we were not able to get a good fit of the spectrum in one of the spectral regions due to a low S/N ratio or non-detection of the absorption lines.

Object	Hubble type	Nuclear Activity	σ_{CO}(km s^{-1})	σ_{CaT}(km s^{-1})	h_{3CO}	h_{3CaT}	h_{4CO}	h_{4CaT}	Conf.
NGC 205	dE5 pec	–	40.7 ± 35.3[a]	98.3 ± 5.3[a]	0.00 ± 0.15	0.00 ± 0.05	0.01 ± 0.12	−0.13 ± 0.03	b
NGC 266	SB(rs)ab	L1.9	204.4 ± 8.2	248.5 ± 26.3	0.00 ± 0.02	0.04 ± 0.07	0.07 ± 0.03	0.01 ± 0.08	a
NGC 315	E+:	L1.9	322.9 ± 5.5	362.0 ± 15.0	0.02 ± 0.02	0.03 ± 0.04	−0.08 ± 0.02	−0.20 ± 0.03	a
NGC 404	SA(s)0-:	L2	55.0 ± 18.4[a]	74.5 ± 22.5	−0.02 ± 0.13	−0.02 ± 0.19	0.03 ± 0.20	−0.03 ± 0.16	a
NGC 410	E+:	T2	276.4 ± 20.0	–	−0.05 ± 0.05	–	−0.03 ± 0.06	–	a
NGC 474	(R')SA(s)0	L2:	164.8 ± 5.4	178.7 ± 7.5	0.03 ± 0.02	0.06 ± 0.04	0.06 ± 0.02	−0.05 ± 0.04	a
NGC 660	SB(s)a pec	T2/H	164.7 ± 17.3	–	−0.05 ± 0.06	–	0.12 ± 0.07	–	b
NGC 1052	E4	L1.9	220.3 ± 4.1	250.6 ± 22.3	−0.01 ± 0.01	−0.07 ± 0.05	0.03 ± 0.01	0.04 ± 0.06	a
NGC 1167	SA0-	S2	179.0 ± 6.2	160.6 ± 41.7	0.01 ± 0.02	0.03 ± 0.06	0.00 ± 0.03	0.00 ± 0.21	a
NGC 1358	SAB(r)0/a	S2	182.3 ± 6.8	174.3 ± 21.2	−0.03 ± 0.03	0.08 ± 0.10	−0.03 ± 0.03	−0.09 ± 0.09	a
NGC 1961	SAB(rs)c	L2	189.9 ± 9.2	249.7 ± 13.9	0.01 ± 0.02	0.03 ± 0.05	0.11 ± 0.03	−0.07 ± 0.04	b
NGC 2273[b]	SB(r)a:	S2	105.7 ± 14.4	142.4 ± 8.3	−0.11 ± 0.06	0.05 ± 0.04	0.03 ± 0.09	0.02 ± 0.05	b
NGC 2639	(R)SA(r)a?	S1.9	160.4 ± 5.2	–	0.02 ± 0.02	–	−0.04 ± 0.03	–	a
NGC 2655	SAB(s)0/a	S2	145.8 ± 6.5	181.1 ± 7.1	0.02 ± 0.02	0.03 ± 0.03	0.08 ± 0.03	0.01 ± 0.03	b
NGC 2768	E6:	L2	172.8 ± 3.8	177.3 ± 6.7	0.01 ± 0.01	−0.05 ± 0.03	0.02 ± 0.02	0.04 ± 0.03	a
NGC 2832	E+2:	L2:	328.7 ± 7.1	254.2 ± 16.9	0.06 ± 0.02	0.02 ± 0.05	−0.01 ± 0.02	−0.03 ± 0.05	b
NGC 3031	SA(s)ab	S1.5	182.5 ± 3.8	149.8 ± 7.1	0.00 ± 0.01	0.04 ± 0.03	0.08 ± 0.01	0.03 ± 0.04	a
NGC 3079	SB(s)c spin	S2	143.6 ± 4.7	–	−0.01 ± 0.02	–	0.05 ± 0.02	–	a
NGC 3147	SA(rs)bc	S2	229.1 ± 4.2	250.2 ± 11.7	0.00 ± 0.01	0.02 ± 0.03	0.06 ± 0.01	0.03 ± 0.03	b
NGC 3169	SA(s)a pec	L2	169.4 ± 4.0	191.6 ± 17.5	0.01 ± 0.02	0.13 ± 0.04	0.01 ± 0.02	0.04 ± 0.06	a
NGC 3190	SA(s)a pec spin	L2	189.2 ± 3.9	202.9 ± 13.6	0.02 ± 0.01	0.00 ± 0.06	0.06 ± 0.01	−0.07 ± 0.05	a
NGC 3607	SA(s)0:	L2	213.5 ± 3.6	201.0 ± 13.9	0.01 ± 0.01	0.00 ± 0.07	0.06 ± 0.01	−0.09 ± 0.06	a
NGC 3718	SB(s)a pec	L1.9	192.7 ± 5.1	224.0 ± 8.4	−0.03 ± 0.01	−0.04 ± 0.03	0.08 ± 0.02	−0.01 ± 0.03	b
NGC 3998	SA(s)ab	L1.9	346.9 ± 5.9	331.5 ± 17.7	0.02 ± 0.01	−0.03 ± 0.04	−0.02 ± 0.02	0.03 ± 0.04	b
NGC 4203	SAB0-:	L1.9	176.4 ± 5.9	182.2 ± 8.4	0.00 ± 0.02	−0.02 ± 0.04	0.03 ± 0.02	−0.05 ± 0.04	b
NGC 4235	SA(s)a spin	S1.2	209.6 ± 13.5	156.4 ± 12.3	−0.10 ± 0.03	0.01 ± 0.05	0.12 ± 0.03	0.06 ± 0.05	b
NGC 4258	SAB(s)b	S1.9	129.6 ± 3.2	132.4 ± 6.4	−0.02 ± 0.01	−0.02 ± 0.04	0.02 ± 0.02	−0.05 ± 0.04	a
NGC 4346	SA0 spin	L2:	124.1 ± 7.4	154.4 ± 6.5	0.00 ± 0.02	0.06 ± 0.02	0.07 ± 0.04	0.00 ± 0.03	b
NGC 4388[b]	SA(s)b: spin	S1.9	103.3 ± 12.4	165.3 ± 20.8	−0.01 ± 0.05	0.01 ± 0.09	0.01 ± 0.08	0.01 ± 0.09	b
NGC 4450	SA(s)ab	L1.9	118.8 ± 4.6	136.4 ± 10.9	0.00 ± 0.02	−0.07 ± 0.05	0.08 ± 0.03	−0.05 ± 0.07	a
NGC 4548	SB(rs)b	L2	104.0 ± 8.8	131.6 ± 6.8	0.00 ± 0.03	0.00 ± 0.04	0.04 ± 0.06	0.02 ± 0.04	b
NGC 4565	SA(s)b? spin	S1.9	151.6 ± 4.0	180.0 ± 5.0	0.03 ± 0.01	−0.01 ± 0.02	0.02 ± 0.02	−0.04 ± 0.02	b
NGC 4569	SAB(rs)ab	T2	106.4 ± 7.6	178.2 ± 7.8	−0.05 ± 0.03	0.08 ± 0.02	0.03 ± 0.05	0.05 ± 0.03	b
NGC 4579	SAB(rs)b	S1.9/L1.9	177.5 ± 5.3	174.9 ± 10.8	0.05 ± 0.02	0.03 ± 0.04	0.06 ± 0.02	0.01 ± 0.05	a
NGC 4594	SA(s)a spin	L2	253.9 ± 3.6	271.4 ± 6.3	0.00 ± 0.01	0.03 ± 0.02	0.06 ± 0.01	−0.01 ± 0.02	b
NGC 4725	SAB(r)ab pec	S2:	133.5 ± 3.3	162.4 ± 11.3	−0.05 ± 0.02	0.27 ± 0.08	−0.02 ± 0.02	−0.27 ± 0.07	a
NGC 4736	(R)SA(r)ab	L2	120.2 ± 6.9	135.4 ± 10.0	0.13 ± 0.04	0.01 ± 0.05	−0.05 ± 0.04	0.01 ± 0.06	b
NGC 4750	(R)SA(rs)ab	L1.9	105.9 ± 11.5	155.9 ± 7.3	−0.01 ± 0.03	−0.05 ± 0.04	0.08 ± 0.07	−0.08 ± 0.04	b
NGC 5005	SAB(rs)bc	L1.9	153.3 ± 6.4	183.1 ± 7.5	−0.01 ± 0.02	−0.01 ± 0.02	0.08 ± 0.03	0.06 ± 0.03	b
NGC 5033	SA(s)c	S1.5	151.0 ± 10.7	147.0 ± 32.7	−0.12 ± 0.04	0.04 ± 0.16	0.15 ± 0.05	−0.01 ± 0.22	a
NGC 5194	SA(s)bc pec	S2	56.3 ± 8.0[a]	91.8 ± 7.0	−0.02 ± 0.0	−0.04 ± 0.05	0.03 ± 0.09	−0.01 ± 0.05	a
NGC 5371	SAB(rs)bc	L2	142.8 ± 6.6	159.3 ± 6.8	−0.01 ± 0.02	0.01 ± 0.03	0.04 ± 0.03	−0.03 ± 0.04	b
NGC 5850	SB(r)b	L2	118.0 ± 8.5	179.3 ± 7.2	0.05 ± 0.03	0.02 ± 0.03	0.07 ± 0.05	−0.05 ± 0.03	b
NGC 6500	SAab:	L2	177.5 ± 5.6	–	0.00 ± 0.02	–	0.04 ± 0.02	–	a
NGC 7217	(R)SA(r)ab	L2	125.8 ± 5.9	157.6 ± 5.6	−0.01 ± 0.02	0.04 ± 0.02	0.03 ± 0.03	0.00 ± 0.03	b
NGC 7331	SA(s)b	T2	137.3 ± 3.2	141.3 ± 6.6	0.03 ± 0.01	−0.03 ± 0.04	0.01 ± 0.02	−0.05 ± 0.04	a
NGC 7743	(R)SB(s)0+	S2	90.2 ± 4.8	133.4 ± 4.8	0.04 ± 0.02	−0.13 ± 0.04	0.05 ± 0.04	−0.20 ± 0.03	a

[a]The measured σ is smaller than the instrumental σ.
[b]The second CO band was excluded from the fitting due to contamination by the [Ca VIII] 2.322 μm emission.

cosmic ray-like features arising from α particles in the camera lens coatings. The files are divided by a flat-field and sky-subtracted using blank sky exposures made between the on-source observations, and then rectified using pinhole images. Wavelength calibration is achieved using argon arc spectra, and then a spectrum of each order is extracted, divided by a standard star to cancel telluric absorption lines, and roughly flux-calibrated using the telluric standard star spectrum. The individual orders are then combined to produce the final spectrum. The extraction aperture used for this work was 1.8 arcsec along the 0.3 arcsec slit, corresponding to a few tens to a few hundreds of parsecs at the distances of these galaxies.

3 METHODS

In order to obtain the line-of-sight velocity distribution (LOSVD), we have used the Penalized Pixel-Fitting (PPXF) method of Cappellari & Emsellem (2004) to fit the CO absorption band heads around 2.3 μm in the *K* band and the Ca II λλ8500, 8544, 8665 (the CaT) stellar absorptions in the *Z* band. The best fit of the galaxy spectrum is obtained by convolving template stellar spectra with the corresponding LOSVD, assumed to be well represented by Gauss–Hermite series. The PPXF method outputs the radial velocity, velocity dispersion (σ), and higher order Gauss–Hermite moments (h_3 and h_4), as well as the uncertainties for each parameter. The h_3 and h_4 moments measure deviations of the LOSVD from a Gaussian curve: the parameter h_3 measures asymmetric deviations (e.g. wings) and the h_4 quantifies the peakiness of the profile, with $h_4 > 0$ and $h_4 < 0$ indicating narrower and broader profiles than Gaussian, respectively (van der Marel & Franx 1993; Riffel 2010).

The dominant source of error in the velocity dispersion is usually related to the choice of stellar template used to fit the galaxy spectrum (e.g. Barth, Ho & Sargent 2002b; Riffel et al. 2008; Winge, Riffel & Storchi-Bergmann 2009). This can be minimized by using a large stellar template library, instead of the spectrum of a single star. The PPXF allows the use of several stellar template spectra, and varies the weighting of each one to obtain the best match to the observed spectrum, minimizing issues arising from template mismatches. The set of templates must include stars that closely match the fitted galaxy spectrum (e.g. Silge & Gebhardt 2003; Emsellem et al. 2004; Riffel et al. 2008). For the fitting of the CO absorptions, we used as template spectra those of the Gemini NIR late-type stellar library (Winge et al. 2009), which contains spectra of 60 stars with spectral types ranging from F7III to M5III, observed in the *K* band at a spectral resolution of ∼3.2 Å (FWHM).

As template spectra for the CaT region, we used selected spectra of stars from the CaT stellar library of Cenarro et al. (2001) with a spectral resolution of 1.5 Å (FWHM). This library contains spectra of 706 stars with all spectral types and is part of the Medium-resolution Isaac Newton Telescope library (MILES; Sánchez-Blázquez et al. 2006). In this work, we used only the spectra of stars with signal-to-noise (S/N) ratio larger than 50 in the CaT region in order to avoid the selection of noisy spectra by the PPXF code. The final template library contains 190 spectra, including several spectral types. We also tested the NASA InfraRed Telescope Facility (IRTF) stellar spectral library (Cushing, Rayner & Vacca 2005; Rayner, Cushing & Vacca 2009) that presents spectra of late-type stars ranging from 0.8 to 5.5 μm at a spectral resolving power of $R = \lambda/\Delta\lambda \sim 2000$, similar to the spectral resolution used in this work. The comparisons of the kinematic parameters obtained with the IRTF spectral library are similar to the ones obtained with the two libraries mentioned above. However, the standard deviation of the residuals (defined as the difference between the galaxy spectrum and the best-fitting model) and the uncertainties are much larger using the IRTF library. This may be related to the S/N ratio of the IRTF spectra, and/or their lower spectral resolution compared to the MILES library. We therefore decided to use the Gemini and MILES libraries for this work.

Since the spectral resolution of the template stellar spectra for both spectral regions is better than the resolution of our observations, we degraded the stellar templates to the same resolution as the spectra of the galaxies before running the PPXF to measure the LOSVD. In order to properly fit the continuum emission, we allowed PPXF to fit multiplicative Legendre polynomials of order 1 to account for any slope introduced by dust/AGN emission. Since the order of the polynomials included is small, they do not introduce any bias in the derived stellar kinematics.

Although PPXF outputs the errors of the measurements, we also performed 100 iterations of Monte Carlo simulations where random noise was introduced to the galaxy spectrum, keeping constant the S/N ratio and the standard deviation of the 100 measurements for each galaxy. The errors obtained from the simulations are similar to the uncertainties that PPXF outputs.

Fig. A1 shows the fits of the galaxy spectra at the region of the CO band heads (2.25–2.41 μm) for all the galaxies of our sample. The fits reproduce the observed spectra very well for all objects, with the residuals being smaller than three times the standard deviation of the continuum emission next to the CO absorptions. Two objects (NGC 2273 and NGC 4388) present strong [Ca VIII] 2.322 μm line emission superimposed on the second ^{12}CO absorption band head, so this band was excluded from the fitted region.

The fits for the CaT spectral region (8480–8730 Å) are shown in Fig. A2. They also reproduce the observed spectra well, with the residuals again generally being smaller than three times the standard deviation of the continuum emission next to the CaT. However, for some objects, the residuals are somewhat larger (e.g. NGC 5194, NGC 5371, NGC 7743, and NGC 7332 – see the bottom panels of Fig. A2) due to the lower S/N ratio of those spectra in this region. This results in uncertainties of up to 25 km s^{-1} in the resulting velocity dispersions.

For the CO spectral region, we find that σ_{CO} is smaller than the spectral resolution of the spectra for three objects (NGC 205, NGC 404, and NGC 5194), while for the CaT region, only the dwarf elliptical NGC 205 has σ smaller than the resolution. These values are marked by ⋆ in Table 1 and should be considered highly uncertain. In particular, for the galaxies NGC 205 and NGC 404, Ho et al. (2009) measured values lower than our resolution, using higher resolution data.

4 RESULTS

The major difference and main advantage of the present work, compared to previous studies, is that we measure both σ_{CO} and σ_{CaT} from the same spectra, observed in the same way, with the same aperture and using the same method, while previous studies used their own σ_{CO} measurements and compared them with optical σ values from the literature. Resulting measurements of the stellar velocity dispersion and Gauss–Hermite moments for our sample are shown in Table 1.

In Fig. 1, we show σ_{CO} versus σ_{CaT}, excluding objects for which good fits could not be obtained for one of the spectral regions (marked by dashes in the Table 1). We find that σ_{CaT} tends to be higher than σ_{CO}, with an average difference of $\sigma_{CO} - \sigma_{CaT} = -19.2 \pm 5.6$ km s^{-1} (for all morphological types). The error in this value was obtained using Monte Carlo simulations and the bootstrap technique (e.g. Beers, Flynn & Gebhardt 1990) as follows. First, 10 000 Monte Carlo iterations were run to determine the effect to the uncertainties in σ to the mean sigma difference ($\langle\sigma_{CO} - \sigma_{CaT}\rangle$). At each run, random values for σ_{CO} and σ_{CaT} constrained to be within their measured uncertainties were generated and then the $\langle\sigma_{CO} - \sigma_{CaT}\rangle$ was calculated. The standard deviation of the 10 000 simulations of $\langle\sigma_{CO} - \sigma_{CaT}\rangle$ (ϵ_{σ_u}) represents the effects of the uncertainties in σ to the $\langle\sigma_{CO} - \sigma_{CaT}\rangle$. Then, to evaluate the completeness of the sample and its effect to the mean σ difference, we run a bootstrap with 10 000 realizations in which for each iteration, the $\langle\sigma_{CO} - \sigma_{CaT}\rangle$ is calculated for a sample selected randomly among the galaxies of our sample. The standard deviation

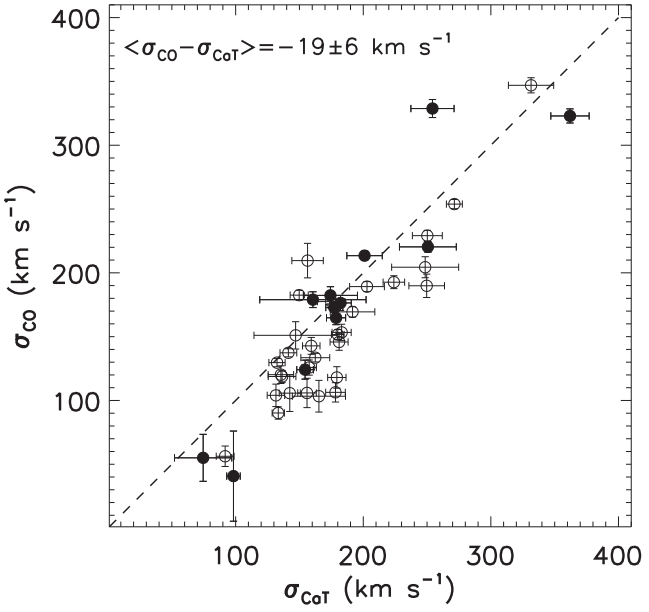

Figure 1. Comparison between the stellar velocity dispersion obtained from the fitting of the CO band heads (*y*-axis) and from the fitting of the CaT (*x*-axis). The dashed line shows a one-to-one relation. Filled circles are for the elliptical and lenticular galaxies of our sample and open circles represent the spiral galaxies.

of the simulated $\langle\sigma_{\rm CO} - \sigma_{\rm CaT}\rangle$ ($\epsilon_{\sigma_{\rm s}}$) represents the intrinsic scatter of our sample. Finally, the uncertainty $\epsilon_{\langle\sigma_{\rm CO}-\sigma_{\rm CaT}\rangle}$ is obtained by the sum of $\epsilon_{\sigma_{\rm u}}$ and $\epsilon_{\sigma_{\rm s}}$ in quadrature, as $\epsilon_{\langle\sigma_{\rm CO}-\sigma_{\rm CaT}\rangle} = \sqrt{(\epsilon^2_{\sigma_{\rm u}} + \epsilon^2_{\sigma_{\rm s}})} = \sqrt{(2.6\,{\rm km\,s^{-1}})^2 + (4.6\,{\rm km\,s^{-1}})^2} = 5.6\,{\rm km\,s^{-1}}$. This value is similar to the standard error. If we exclude also the three objects with σ values smaller than the instrumental broadening, we find $\sigma_{\rm CO} - \sigma_{\rm CaT} = -17.7 \pm 5.7\,{\rm km\,s^{-1}}$.

We also performed a Kolmogorov–Smirnov test to determine if $\sigma_{\rm CaT}$ and $\sigma_{\rm CO}$ differ significantly. We found a statistic significance $P = 0.2$ for our sample, where P ranges from 0 to 1 and small values mean that the two data sets are significantly different. The value of P obtained for our sample indicates that there is a reasonable probability (80 per cent) that $\sigma_{\rm CaT}$ and $\sigma_{\rm CO}$ present discrepant values.

The comparisons of higher order Gauss–Hermite moments h_3 and h_4 obtained from the fitting of the CaT with those of the CO band heads show an average differences of $h_{3\rm CO} - h_{3\rm CaT} = -0.01 \pm 0.03$ and h_4 is $h_{4\rm CO} - h_{4\rm CaT} = 0.07 \pm 0.03$. For both the h_3 and h_4 parameters, there is no correlation between the values found from the fitting of the CaT and the ones from the CO band heads. The values found for h_3 and h_4 are small for most of the objects in our sample, indicating that the LOSVD of the stars for the nucleus of these galaxies is reasonably well reproduced by a Gaussian velocity distribution.

5 ANALYSIS OF THE RESULTS

To understand the observed difference between $\sigma_{\rm CO}$ and $\sigma_{\rm CaT}$ in the galaxies, we performed several tests to identify possible systematic effects in the data or introduced by the fitting procedure.

As discussed in Section 3, we were very careful in the estimation of the instrumental broadening, taking into account the facts that (i) our observations present distinct spectral resolutions depending on the date of the observations, and (ii) the spectral resolution for observations performed after 2012 November differs between the CaT and CO regions (Section 2). The uncertainty (rms) in the FWHM of the arc lamp lines is smaller than 10 km s^{-1} for both spectral regions, and in order to 'correct' the offset from the one-to-one relation observed in σ in Fig. 1, the FWHM in the CaT region would have to be underestimated by more than 30 km s^{-1}. Thus, uncertainties in the instrumental broadening cannot account for the observed differences in CaT- and CO-based σ values in our sample.

As noted in Section 3, template mismatch could also introduce systematic uncertainties in the σ measurements (e.g. Silge & Gebhardt 2003; Riffel et al. 2008). Usually fewer than 10 template spectra are needed by PPXF to successfully reproduce the CO absorption band heads and the CaT. Although the libraries used here are large and contain spectra of stars with several spectral types, the fits to both spectral regions are dominated by giant and supergiant stars, with a slightly larger contribution from supergiants in the *K* band. These are the spectral types that are expected to dominate the emission in the NIR, suggesting that PPXF is selecting the appropriate stars with which to fit the spectra. For most galaxies, M-stars are the dominant contributor to the fits in the *K* band, while K-stars dominate in the region of the CaT. The difference between the intrinsic widths of the absorption lines in these stars is ∼10 km s^{-1}, which is negligible compared to the overall difference between $\sigma_{\rm CaT}$ and $\sigma_{\rm CO}$ in the sample. In Appendix B, we show the stellar templates used to fit the spectrum of each galaxy. Additionally, there is no difference in the χ^2 values of the fits between early- and late-type galaxies, suggesting that there is no bias in the choice of template for each type of galaxy.

As several galaxies of our sample have a Seyfert nucleus, hot dust emission may play an important role in the *K*-band continuum. The CO band heads can be 'diluted' by this emission, which might introduce an uncertainty in the measurements of $\sigma_{\rm CO}$ (e.g. Ivanov et al. 2000; Riffel, Rodríguez-Ardila & Pastoriza 2006; Kotilainen et al. 2012). To test whether the PPXF accounts correctly for variations of the continuum shape, we have simulated contributions of Planck functions with temperatures ranging from 700 to 2000 K to the continuum emission at the *K* band. No significant difference in $\sigma_{\rm CO}$ was found when including dust emission ranging from 1 to 70 per cent of the total *K*-band emission. Furthermore, for the objects in which we could measure the σ from the *H*-band CO lines (where the contribution from AGN-heated dust is smaller; Origlia, Moorwood & Oliva 1993), it agrees to within 10 per cent with that measured from the *K* band and no systematic difference is found between *H*- and *K*-band measurements. Thus, we conclude that the hot dust emission plays a negligible role in the σ measurements.

In galaxies with low values of σ, the fitting of higher order Gauss–Hermite moments can introduce uncertainties in the σ measurements (see the *bias* parameter of the PPXF program; Cappellari & Emsellem 2004). To test this, we fitted the spectra of the galaxies assuming that the LOSVD is well described by a Gaussian, by fitting only the first two moments. In Fig. 2, we present the comparison of σ values obtained from the fitting of four moments with those obtained from the fitting of two moments. This figure shows that the resulting σ for both the CO and CaT spectral regions are very similar to those obtained when allowing the PPXF to include the h_3 and h_4 parameters, suggesting that the inclusion of these parameters does not affect significantly the σ measurements for our sample.

Finally, we compare our $\sigma_{\rm CaT}$ measurements with the optical σ values of Ho et al. (2009) for the same galaxies. Ho et al. (2009) used two spectral ranges to measure σ: a blue region, from 4200 to 5000 Å that includes several Fe lines, and a red region, covering the

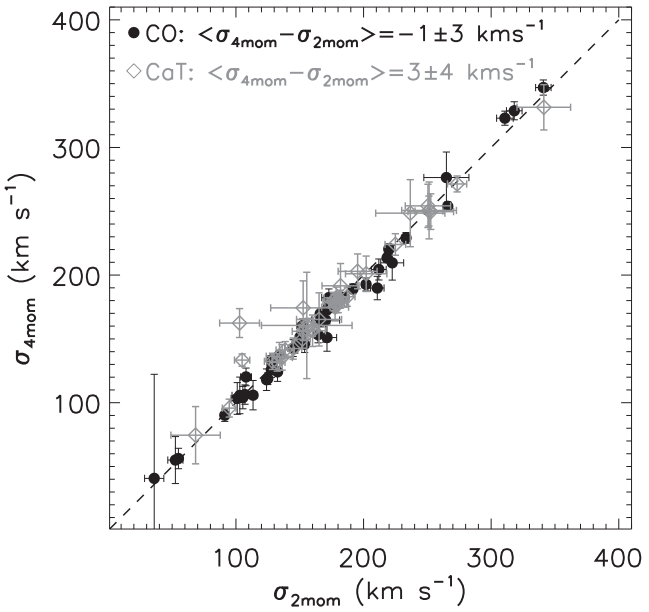

Figure 2. Comparison of σ values obtained from the fit of two and four moments in the LOSVD.

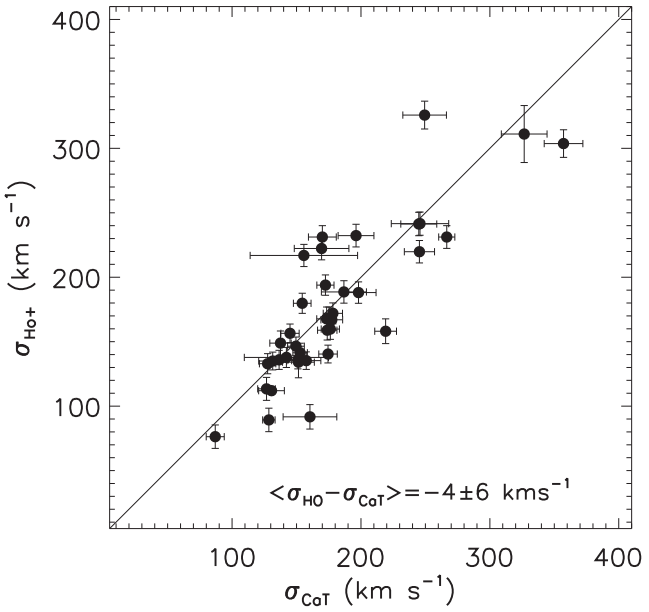

Figure 3. Comparison of $\sigma_{\rm CaT}$ with those found by Ho et al. (2009) using various optical lines.

range 6450–6550 Å where Ca+Fe lines are present. They found that both values are in good agreement. In Fig. 3, we show our $\sigma_{\rm CaT}$ versus the σ values presented in Ho et al. (2009). This comparison shows that 50 per cent of the objects have σ differences smaller than 10 per cent and for about 90 per cent of the objects the differences are smaller than 25 per cent, indicating that our measurements are in agreement with those from Ho et al. (2009). Differences between the measurements may be due to the larger aperture (2 arcsec × 4 arcsec) used by Ho et al. (2009), as well as differences in the S/N ratio of the spectra and the exact measurement procedures used.

We therefore conclude that our σ measurements are robust, and that the observed difference between $\sigma_{\rm CaT}$ and $\sigma_{\rm CO}$ is not due to measurement error.

6 DISCUSSION

We have found a systematic offset between $\sigma_{\rm CO}$ and $\sigma_{\rm CaT}$ in the galaxies in our sample, which are primarily spirals. In order to further investigate the σ-discrepancy in late-type galaxies and compare the results with the available studies of other galaxy types, we compiled values for the $\sigma_{\rm CO}$ and for optical measurements (most of them obtained from the CaT region) from the literature for distinct classes of objects. Table 2 presents the resulting $\sigma_{\rm opt}$ and $\sigma_{\rm CO}$ values for elliptical, lenticular and spiral galaxies, and merger remnants. Since there is good agreement between the σ values obtained from CaT and those from the fitting of other optical lines (e.g. Barth, Ho & Sargent 2002a; Barth et al. 2002b) and as not all the optical values from the literature were obtained from the CaT region, we will use the nomenclature 'optical' velocity dispersion ($\sigma_{\rm opt}$) to refer to measurements of σ obtained from the CaT or other optical lines.

In order to investigate the relation between σ-discrepancy and morphological classification, we plotted in Fig. 4 $\sigma_{\rm opt}$ versus $\sigma_{\rm CO}$ for distinct classes of objects. The largest σ difference is observed for the merger remnants and ULIRGs, for which no correlation is found between $\sigma_{\rm opt}$ and $\sigma_{\rm CO}$ and the mean difference is $\sigma_{\rm CO} - \sigma_{\rm opt} = -57.8 \pm 13.7$ km s^{-1}. Elliptical galaxies follow the one-to-one relation and no discrepancy between optical and NIR measurements is found. The mean difference is $\sigma_{\rm CO} - \sigma_{\rm opt} = -1.5 \pm 4.6$ km s^{-1}. For lenticulars, the mean difference is $\sigma_{\rm CO} - \sigma_{\rm opt} = -10.8 \pm 6.4$ km s^{-1} and it can be seen from the figure that most points are distributed around the one-to-one relation. The best linear fit for lenticular galaxies is given by

$$\sigma_{\rm opt} = (9.1 \pm 13.2) + (0.99 \pm 0.08)\sigma_{\rm CO}, \quad (1)$$

shown as a dashed line in the bottom-left panel of Fig. 4.

For spiral galaxies, we found a mean difference of $\sigma_{\rm CO} - \sigma_{\rm opt} = -24.0 \pm 4.9$ km s^{-1}. Excluding NGC 5194, which presents a sigma value smaller than the spectral resolution of the data, we find the same relation, with $\epsilon_{\langle\sigma_{\rm CO}-\sigma_{\rm CaT}\rangle} = 5.0$ km s^{-1}. Most objects have σ smaller than 200 km s^{-1} and for these objects $\sigma_{\rm CO}$ is clearly smaller than $\sigma_{\rm opt}$.

The best linear equation for spiral galaxies is

$$\sigma_{\rm opt} = (46.0 \pm 18.1) + (0.85 \pm 0.12)\sigma_{\rm CO}, \quad (2)$$

where we excluded from the fit the galaxy NGC 5194 (identified in Fig. 4). The main cause of uncertainty in equation (2) is the small range of σ probed by the observations. Further observations are needed to cover the high-σ region ($\sigma \gtrsim 220$ km s^{-1}), and higher spectral resolution observations of objects with $\sigma \lesssim 100$ km s^{-1}, in order to improve the calibration of the equation above.

We therefore observe that $\sigma_{\rm CO}$ and $\sigma_{\rm opt}$ become both more similar and more correlated in early-type galaxies compared with spirals and ULIRGs/merger remnants.

6.1 What is the origin of the sigma discrepancy for late-type galaxies?

As discussed above and in Section 1, the discrepancy between the stellar velocity dispersion obtained from optical bands and that obtained from the NIR CO absorption band heads is larger for mergers of galaxies and ULIRGs than for early-type galaxies. Rothberg & Fischer (2010) found a correlation between the infrared luminosity ($L_{\rm IR}$) and $\sigma_{\rm frac}$ for merger remnants, while no correlation is found for elliptical galaxies. Rothberg et al. (2013) showed that the correlation found for merger remnants extends to ULIRGs, suggesting

Table 2. Velocity dispersions compiled from the literature.

Object	σ_{CO}(km s^{-1})	σ_{opt}(km s^{-1})	Ref.	Object	σ_{CO}(km s^{-1})	σ_{opt}(km s^{-1})	Ref.
Elliptical galaxies						Lenticular galaxies	
NGC 221	71 ± 8	75 ± 4	[1]	NGC 1023	152 ± 11	205 ± 10	[1]
	70 ± 2	75 ± 3	[2]		217 ± 5	205 ± 10	[2]
	60 ± 8	69 ± 2	[4]	NGC 1161	274 ± 19	297 ± 17	[1]
NGC 315	321 ± 59	310 ± 16	[1]	NGC 1375	64 ± 4	56 ± 10	[3]
	324 ± 59	351 ± 16	[4]	NGC 1380	190 ± 17	219 ± 11	[3]
NGC 821	195 ± 17	209 ± 10	[1]	NGC 1380A	60 ± 9	55 ± 9	[3]
	208 ± 5	209 ± 10	[2]	NGC 1381	155 ± 6	153 ± 8	[3]
	188 ± 17	197 ± 20	[4]	NGC 1400	212 ± 12	264 ± 26	[1]
NGC 1052	211 ± 20	196 ± 4	[4]	NGC 2110	224 ± 49	220 ± 25	[1]
NGC 1316	212 ± 20	243 ± 9	[4]	NGC 2293	255 ± 44	254 ± 13	[1]
NGC 1336	119 ± 8	96 ± 5	[3]	NGC 2380	164 ± 31	189 ± 9	[1]
NGC 1339	182 ± 9	158 ± 8	[3]	NGC 2681	82 ± 9	111 ± 22	[1]
NGC 1344	158 ± 20	166 ± 7	[4]	NGC 2768	235 ± 51	198 ± 28	[1]
NGC 1351	153 ± 7	157 ± 8	[3]	NGC 2787	153 ± 8	210 ± 12	[1]
NGC 1373	80 ± 5	75 ± 4	[3]		186 ± 3	189 ± 9	[2]
NGC 1374	207 ± 10	185 ± 9	[3]	NGC 3115	272 ± 12	230 ± 11	[2]
	181 ± 20	180 ± 8	[4]	NGC 3245	206 ± 7	205 ± 10	[2]
NGC 1379	130 ± 7	130 ± 7	[3]	NGC 3384	151 ± 3	143 ± 7	[2]
	126 ± 20	127 ± 5	[4]	NGC 3998	205 ± 16	297 ± 15	[1]
NGC 1399	406 ± 33	375 ± 19	[3]	NGC 4150	113 ± 18	132 ± 10	[1]
	336 ± 20	325 ± 15	[4]	NGC 4342	224 ± 5	225 ± 11	[2]
NGC 1404	247 ± 22	260 ± 13	[3]	NGC 4564	175 ± 7	162 ± 8	[2]
	204 ± 20	230 ± 10	[4]	NGC 4596	139 ± 3	136 ± 6	[2]
NGC 1407	297 ± 40	283 ± 13	[4]	NGC 5195	95 ± 6	175 ± 30	[1]
	306 ± 40	285 ± 40	[1]	NGC 5866	186 ± 14	139 ± 7	[1]
NGC 1419	125 ± 5	117 ± 6	[3]	NGC 6548	225 ± 47	307 ± 23	[1]
	116 ± 20	110 ± 6	[4]	NGC 6703	146 ± 42	186 ± 9	[1]
NGC 1427	155 ± 18	175 ± 9	[3]	NGC 7332	148 ± 13	130 ± 10	[1]
	174 ± 20	172 ± 8	[4]	NGC 7457	63 ± 2	67 ± 3	[2]
NGC 2778	161 ± 4	175 ± 8	[2]	NGC 7743	66 ± 12	83 ± 20	[1]
NGC 2974	272 ± 19	262 ± 13	[1]	IC 1963	49 ± 6	58 ± 10	[3]
	262 ± 19	255 ± 12	[4]	ESO 358-G06	55 ± 25	58 ± 11	[3]
NGC 3377	144 ± 20	145 ± 7	[1]	ESO 358-G59	70 ± 20	54 ± 9	[3]
	147 ± 4	145 ± 7	[2]		SPIRAL GALAXIES		
	134 ± 20	135 ± 4	[4]	NGC 1068	129 ± 3	151 ± 7	[2]
NGC 3379	235 ± 20	185 ± 2	[4]	NGC 3031	157 ± 3	143 ± 7	[2]
NGC 3607	210 ± 8	229 ± 11	[2]	NGC 4258	111 ± 2	115 ± 10	[2]
NGC 3608	187 ± 4	182 ± 9	[2]		Merger remnants/ULIRGs		
NGC 4261	286 ± 6	315 ± 15	[2]	NGC 1614	133 ± 3	219 ± 3	[4]
NGC 4291	248 ± 7	242 ± 12	[2]	NGC 2418	245 ± 7	282 ± 3	[4]
NGC 4365	262 ± 20	240 ± 3	[4]	NGC 2623	152 ± 4	174 ± 3	[4]
NGC 4374	290 ± 8	296 ± 14	[2]	NGC 2914	179 ± 6	178 ± 2	[4]
NGC 4459	164 ± 6	167 ± 8	[2]	NGC 3256	111 ± 20	239 ± 4	[4]
NGC 4472	291 ± 20	269 ± 3	[4]	NGC 4194	98 ± 25	103 ± 2	[4]
NGC 4473	186 ± 3	190 ± 9	[2]	NGC 5018	243 ± 7	222 ± 2	[4]
NGC 4486	310 ± 20	361 ± 37	[4]	NGC 7252	119 ± 19	160 ± 3	[4]
	331 ± 11	375 ± 18	[2]	Arp 193	143 ± 5	229 ± 4	[4]
NGC 4649	327 ± 11	385 ± 19	[2]	IC 5298	150 ± 28	187 ± 4	[4]
NGC 4697	172 ± 4	177 ± 8	[2]	AM 0612-373	240 ± 9	286 ± 9	[4]
NGC 4742	104 ± 3	90 ± 5	[2]	AM 1419-263	262 ± 6	258 ± 3	[4]
NGC 5128	190 ± 13	145 ± 6	[4]	AM 2038-382	207 ± 4	256 ± 5	[4]
NGC 5812	230 ± 6	248 ± 2	[4]	AM 2055-425	137 ± 15	207 ± 7	[4]
NGC 5845	237 ± 4	234 ± 11	[2]	IRAS 02021−2103	143 ± 21	209 ± 8	[5]
NGC 6251	290 ± 8	290 ± 14	[2]	IRAS 05189−2524	131 ± 16	265 ± 7	[5]
NGC 7052	327 ± 13	266 ± 13	[2]	IRAS 12540−5708	117 ± 10	346 ± 9	[5]
NGC 7619	246 ± 47	296 ± 15	[1]	IRAS 17208−0014	223 ± 15	261 ± 5	[5]
	246 ± 47	296 ± 11	[4]	IRAS 23365−3604	143 ± 15	221 ± 6	[5]
NGC 7743	66 ± 12	83 ± 20	[1]				
NGC 7626	313 ± 20	265 ± 10	[4]				
IC 2006	125 ± 10	136 ± 7	[3]				

[1] – Silge & Gebhardt (2003); [2] – Kang et al. (2013); [3] – Vanderbeke et al. (2011); [4] – Rothberg & Fischer (2010); [5] – Rothberg et al. (2013).

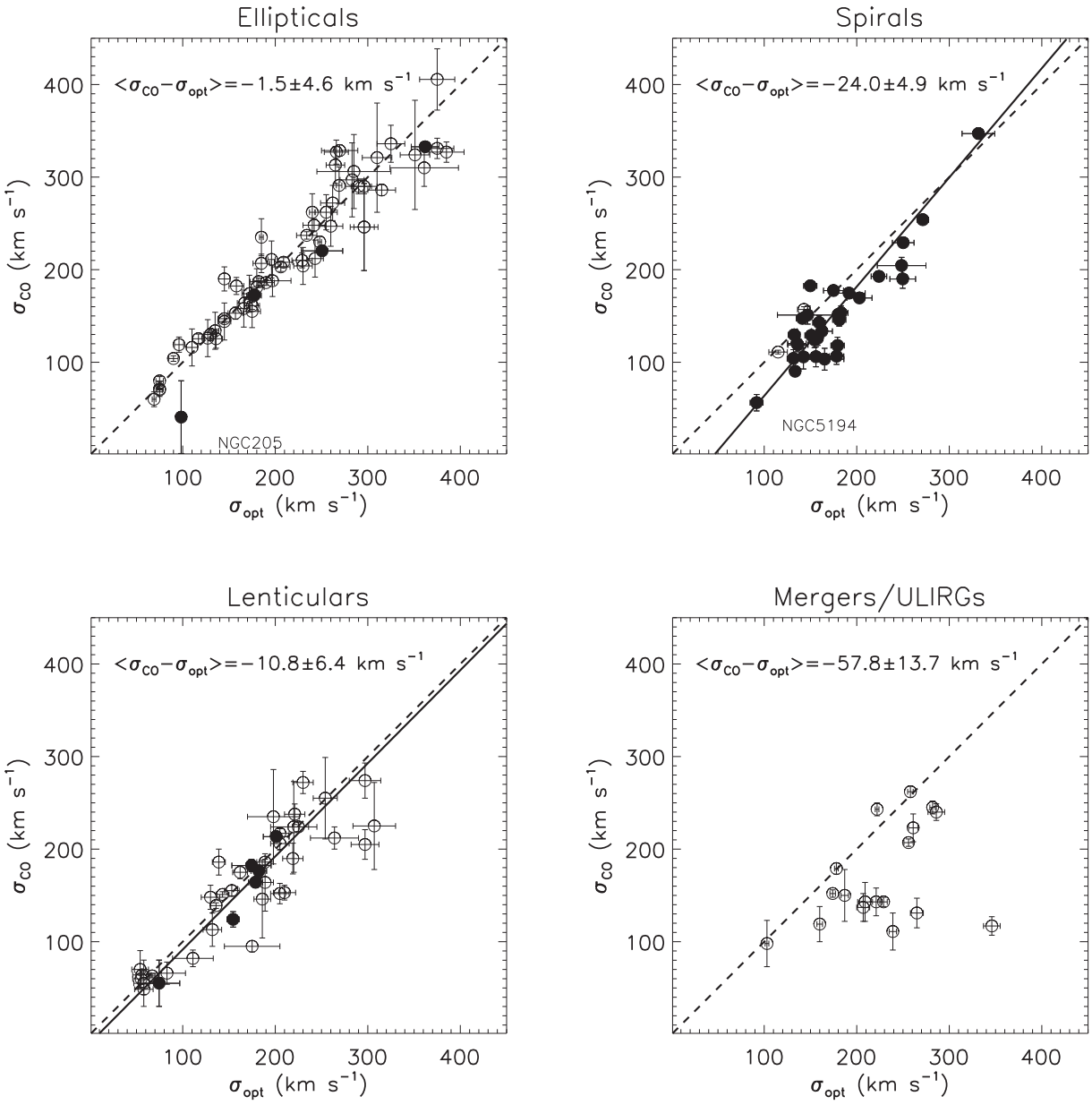

Figure 4. Comparison of the σ values in the NIR with the optical values for distinct morphological types. The objects from our sample are shown as filled circles and open circles are for measurements from the literature. The dashed line shows a one-to-one relation and the continuous line is the best linear fit of the data. NGC 205 and NGC 5194, which have σ smaller than the instrumental resolution, are identified in the plots.

that dust might play an important role in the σ_{CO} values for this kind of object.

Fig. 5 shows a plot of $\sigma_{frac} = \frac{\sigma_{CO}-\sigma_{opt}}{\sigma_{opt}}$ versus log L_{IR} for the galaxies with available IR luminosities [from Ho et al. (1997), Rothberg et al. (2013) and Rothberg & Fischer (2010)]. The values of L_{IR} were estimated using their infrared fluxes F_{IR} from Ho et al. (1997), who defined it as $F_{IR} = 1.26 \times 10^{-14}(2.58S_{60} + S_{100})$ W m^2, S_{60} and S_{100} being the flux densities at 60 and 100 μm, respectively. Although data with higher angular resolution and wider wavelength coverage are now available from *Herschel* and *Spitzer* telescopes, we use the *IRAS* fluxes since they are available for most of our objects, while *Herschel* and *Spitzer* data are still not available for most of them of them (e.g. Marleau et al. 2006; Sauvage et al. 2010; Ciesla et al. 2012; De Looze et al. 2012; Auld et al. 2013). Fig. 5 shows that galaxies with higher L_{IR} also have higher negative values of σ_{frac}, and that the spiral galaxies fill the gap between early-type objects and merger remnants. This smooth trend suggests that dust might play some role in the observed σ-discrepancy, as more warm dust is expected in spiral galaxies than in elliptical galaxies, and less than in merger remnants and ULIRGs.

Following Rothberg & Fischer (2010), we estimate the mass of dust by

$$\frac{M_{dust}}{M_\odot} = 0.959 S_{100} D^2 \left[\left(9.96 \frac{S_{100}}{S_{60}} \right)^{1.5} - 1 \right], \quad (3)$$

where S_{60} and S_{100} are the *IRAS* flux densities at 60 and 100 μm in Jy, respectively, and D is the distance to the galaxy in Mpc (see also Hildebrand 1983; Thuan & Sauvage 1992). Rothberg & Fischer (2010) found that σ_{frac} correlates with M_{dust} for merger remnants,

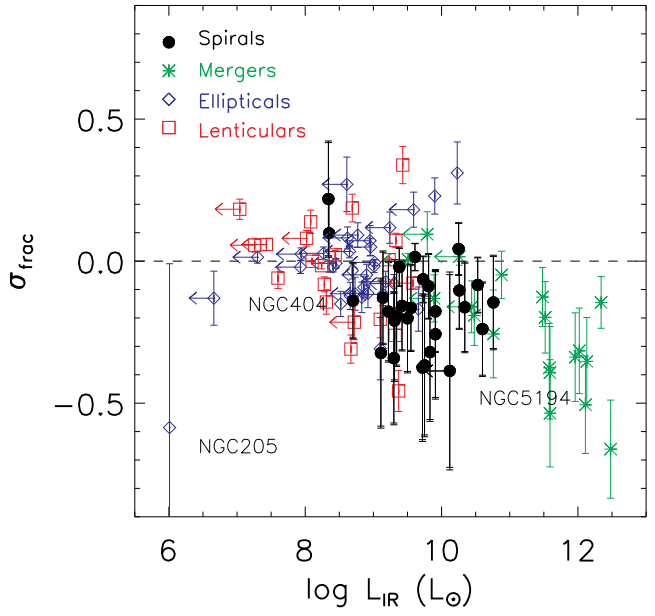

Figure 5. Fractional difference between σ_{CO} and σ_{CaT} ($\sigma_{frac} = \frac{\sigma_{CO}-\sigma_{CaT}}{\sigma_{CaT}}$) versus L_{IR}. The three objects with σ values smaller than the spectral resolution of our data are identified in the plot.

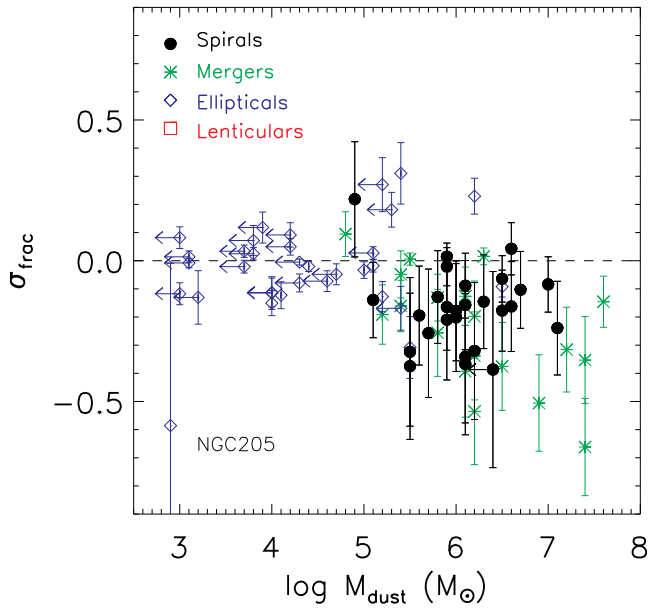

Figure 6. σ_{frac} versus logM_{dust} for distinct types of objects.

while no correlation is found for elliptical galaxies. Fig. 6 shows the plot of σ_{frac} versus M_{dust} for the galaxies studied here. A similar trend to that seen in Fig. 5 is observed in this plot, suggesting that dust plays a role in the observed σ-discrepancy for spirals and merger remnants.

Dust may be relevant to the σ-discrepancy in two ways. First, as extinction is lower in the K band, the σ_{CO} measurements could probe a dynamically cold, disc-like component that is more obscured than the dynamically hot bulge stars. Indeed, NIR studies of nearby galaxies show that the reddening obtained from NIR lines is larger than that obtained from optical lines, indicating that the NIR samples an obscuring column larger than the optical spectral region (e.g. Moorwood & Oliva 1988; Heisler & De Robertis 1999; Martins et al. 2013a). Assuming a standard Galactic extinction curve (Weingartner & Draine 2001; Draine 2003), the extinction at 0.85 μm (CaT) is about a factor of 5 larger than that at 2.3 μm (CO), and the extinction at 0.52 μm (Mg*b*) is about a factor of 2 greater again. If the difference between σ_{CaT} and σ_{CO} is due to extinction, we may also expect a difference between σ_{CaT} and σ_{Mgb}. However, Barth et al. (2002a) compared σ_{CaT} and σ_{Mgb} and did not find any systematic difference between them.

Secondly, warm ($T \sim 50$ K), far-infrared-emitting dust may be associated with star formation in these galaxies. Indeed, the emission of the warm dust is directly correlated with the star formation rate, as it is heated by young stars (Kennicutt 1998; Kennicutt & Evans 2012).

Young stars form in disc, and in the absence of major perturbations generally remain dynamically cold. Indications of young stars in disc have been found in recent spatially resolved spectroscopy of galaxy nuclei with the Near-IR IFU Spectrograph (NIFS) on Gemini North. Riffel et al. (2010, 2011) and Storchi-Bergmann et al. (2012) carried out stellar population synthesis and found a spatial relation between low-σ_{CO} and the young/intermediate-age stellar population, confirming that σ_{CO} is affected by the presence of young/intermediate-age stars. The presence of a young stellar population has also been proposed as an explanation of the σ-drop observed in some galaxies (e.g. Emsellem et al. 2001; Márquez et al. 2003). However, the comparison of our results with spatially resolved measurements should be taken with caution. While the NIFS data resolve a dynamically cold structure, our single-aperture measurements probe the second moment of the LOSVD, which does not necessarily imply a direct link between the two sets of results. New spatially resolved measurements of both the CaT and CO lines would show whether the effect we are observing here is related to the low-σ regions observed in the works cited above.

If the difference between σ_{CO} and σ_{CaT} is due to the presence of a young stellar population in the disc of the galaxies, young stars must contribute more to the CO absorption features than do older stars, and the effect of this population on the σ measured from the CaT and optical lines must be negligible. The connection between the CO and CaT bands and the age of the stellar population is not straightforward, though. For example, the CO bands are relatively strong in both young/intermediate-age stars (AGB/TP-AGB stars) and old ones (M-stars), while hotter, younger stars produce strong CaT bands along with weak CO features (e.g. Maraston 2005; Riffel et al. 2007). On the other hand, previous work has shown that σ_{CaT} is not very sensitive to the stellar population (Barth et al. 2002a, 2002b). Full stellar population synthesis would help to resolve these issues, although different models currently make very different predictions for the NIR spectral region (e.g. Bruzual & Charlot 2003; Maraston 2005).

6.2 Implications for the $M_\bullet$–σ relationship

As discussed above, the σ-discrepancy observed in our sample of mostly late-type galaxies does not appear in previous studies of early-type galaxies. We can use the measured σ values to evaluate the impact of the σ-discrepancy on determinations of the mass of the central SMBH using the $M_\bullet$–σ relationship. Several studies have aimed at properly calibrating the $M_\bullet$–σ relation for distinct classes of objects. Xiao et al. (2011) investigated the $M_\bullet$–σ relation using a sample of 93 late-type galaxies with a Seyfert 1 nucleus. They found

no difference in the slope for subsamples of barred and unbarred galaxies, but they found a small offset in the relation between low- and high-inclination disc galaxies, with the latter having a larger σ value for a given black hole mass. For a review of calibrations of the $M_\bullet$–σ relation, see Kormendy & Ho (2013).

Actually, Kormendy, Bender & Cornell (2011) show that the physically relevant parameter in black hole correlations with host galaxy type is not early-type versus late-type objects, but rather classical bulges versus pseudo-bulges. The latter is defined as the buildup of dense central components that look like classical merger-built bulges but that were in fact formed slowly by disc out of disc material (Kormendy & Kennicutt 2004).

Since the aim of the present paper is to evaluate the impact of the use of CO-based measurements of the stellar velocity dispersion on the derived mass of the SMBH, and not to calibrate the $M_\bullet$–σ relationship, we use the same calibration for all objects of our sample, given by Kormendy & Ho (2013) as

$$\log\left(\frac{M_\bullet}{10^9\,\mathrm{M}_\odot}\right) = -\,(0.500 \pm 0.049) + (4.420 \pm 0.295)\log\left(\frac{\sigma}{200\,\mathrm{km\,s^{-1}}}\right). \quad (4)$$

We estimated the mass of the SMBH for all spiral galaxies of our sample using σ_{CaT} and σ_{CO} in the equation above. The mean logarithmic difference is -0.29 ± 0.12, which may be taken as a systematic error in the $M_\bullet$–σ relation when using CO-based estimates of the stellar velocity dispersion.

7 CONCLUSIONS

We have used 0.85–2.5 μm spectroscopy of a sample of 48 galaxies (35 spirals, 7 lenticulars, and 6 ellipticals) obtained with the GNIRS on Gemini North telescope to measure the stellar kinematics by fitting the *K*-band CO absorption band heads and the CaT at 8550 Å. This work is aimed at determining whether the difference in σ_{CO} and σ_{CaT} (the 'σ-discrepancy') reported for ULIRGs and merger remnants persists in the hitherto unexplored regime of late-type galaxies. Our main conclusions are as follows.

(i) The velocity dispersion obtained from the 2.29 μm CO band heads is slightly smaller than the one from fitting the CaT, with an average difference of $\sigma_{\mathrm{CO}} - \sigma_{\mathrm{CaT}} = -19 \pm 6\ \mathrm{km\,s^{-1}}$ for the complete sample (all morphological types).

(ii) We compiled the available σ values from the literature and found an almost one-to-one relation between optical (CaT, Mg*b*, etc.) and CO-based estimates for early-type galaxies. For spiral galaxies, the discrepancy is higher, but still much lower than for merger remnants. The best fit for spiral galaxies is $\sigma_{\mathrm{opt}} = (46.0 \pm 18.1) + (0.85 \pm 0.12)\sigma_{\mathrm{CO}}$, but more observations covering the σ ranges $\sigma < 100\ \mathrm{km\,s^{-1}}$ and $\sigma > 200\ \mathrm{km\,s^{-1}}$ are needed to properly calibrate this relation.

(iii) The fractional σ difference correlates with the IR luminosity, which may suggest that the σ-discrepancy is related to the presence of warm dust. In this scenario, the CO absorption band heads would be dominated by young stars located in the disc of the galaxy and thus result in smaller σ values, while the optical estimates are less sensitive to variations in the stellar population. However, the detailed spectral synthesis that would be needed to test this interpretation requires high spectral resolution Simple Stellar Populations (SSP) models, which are not yet available.

(iv) We investigated the impact of the σ-discrepancy on the mass of the SMBH obtained via the $M_\bullet$–σ relation and found a mean logarithmic difference of -0.29 ± 0.12, which must be considered as a systematic error in the SMBH mass when using σ_{CO} for spiral galaxies. However, this uncertainty is dominated by scatter of the relation and the conversion from σ_{CO} to σ_{opt} may introduce an even larger uncertainty in the derived $M_\bullet$.

Although the 'σ-discrepancy' has already been discussed for ULIRGs and merger remnants (e.g. Rothberg & Fischer 2010; Rothberg et al. 2013) and no discrepancy was found for early-type galaxies (e.g. Silge & Gebhardt 2003; Vanderbeke et al. 2011; Kang et al. 2013), this is the first time that this comparison is done for a sample of mostly late-type galaxies.

ACKNOWLEDGEMENTS

We thank an anonymous referee for useful suggestions which helped to improve the paper and S. Rembold for help with the bootstrap technique. This work is based on observations obtained at the Gemini Observatory, which is operated by the Association of Universities for Research in Astronomy, Inc., under a cooperative agreement with the NSF on behalf of the Gemini partnership: the National Science Foundation (United States), the Science and Technology Facilities Council (United Kingdom), the National Research Council (Canada), CONICYT (Chile), the Australian Research Council (Australia), Ministério da Ciência, Tecnologia e Inovação (Brazil), and Ministerio de Ciencia, Tecnologia e Innovación Productiva (Argentina). RAR acknowledges support from FAPERGS (project no. 12/1209-6) and CNPq (project no. 470090/2013-8). LCH acknowledges support from the Kavli Foundation, Peking University, and grant no. XDB09030102 (Emergence of Cosmological Structures) from the Strategic Priority Research Program of the Chinese Academy of Sciences. ARA acknowledges CNPq for partial support to this work through grant 307403/2012-2. LM thanks CNPq through grant 305291/2012-2. LC acknowledges support from the Special Visiting Researcher Fellowship (PVE 313945/2013-6) under the Brazilian Scientific Mobility Program 'Ciências sem Fronteiras'. RR acknowledges funding from FAPERGs (ARD 11/1758-5) and CNPq (PeP 304796/2011-5). CRA is supported by a Marie Curie Intra European Fellowship within the 7th European Community Framework Programme (PIEF-GA-2012-327934) and by the Spanish Ministry of Science and Innovation (MICINN) through project PN AYA2010-21887-C04.04.

REFERENCES

Auld R. et al., 2013, MNRAS, 428, 1880
Barth A. J., Ho L. C., Sargent W. L. W., 2002a, ApJ, 124, 2607
Barth A. J., Ho L. C., Sargent W. L. W., 2002b, ApJ, 566, L13
Beers T. C., Flynn K., Gebhardt K., 1990, AJ, 100, 32
Bellovary J., Holley-Bockelmann K., Gültekin K., Christensen C., Governato F., Brooks A., Loebman S., Munshi F., 2014, MNRAS, 445, 2667
Bender R., Burstein D., Faber S. M., 1993, ApJ, 411, 153
Bernardi M. et al., 2003, AJ, 125, 1866
Bower R. G., Benson A. J., Malbon R., Helly J. C., Frenk C. S., Baugh C. M., Cole S., Lacey C. G., 2006, MNRAS, 370, 645
Bruzual G., Charlot S., 2003, MNRAS, 344, 1000
Cappellari M., Emsellem E., 2004, PASP, 116, 138
Cappellari M. et al., 2007, MNRAS, 379, 418
Cenarro A. J., Cardiel N., Gorgas J., Peletier R. F., Vazdekis A., Prada F., 2001, MNRAS, 326, 959
Ciesla L. et al., 2012, A&A, 543, 161
Cox T. J., Dutta S. N., Di Matteo T., Hernquist L., Hopkins P. F., Robertson B., Springel V., 2006, ApJ, 650, 791

Cushing M. C., Rayner J. T., Vacca W. D., 2005, ApJ, 623, 1115
De Looze I. et al., 2012, MNRAS, 423, 2359
Di Matteo T., Springel V., Hernquist L., 2005, Nature, 433, 604
Djorgovski S., Davis M., 1987, ApJ, 313, 59
Draine B. T., 2003, ARA&A, 41, 241
Dressler A., 1984a, ApJ, 281, 512
Dressler A., Lynden-Bell D., Burstein D., Davies R. L., Faber S. M., Terlevich R., Wegner G., 1987, ApJ, 313, 42
Emsellem E., Greusard D., Combes F., Friedli D., Leon S., Pécontal E., Wozniak H., 2001, A&A, 368, 52
Emsellem E. et al., 2004, MNRAS, 352, 721
Falcón-Barroso J. Peletier R. F., Balcells M., 2002, MNRAS, 335, 741
Ferrarese L., Merrit D., 2000, ApJ, 547, 140
Gebhardt K. et al., 2000, ApJ, 539, 13
Gebhardt K. et al., 2003, ApJ, 583, 92
Gültekin K., Cackett E. M., Miller J. M., Di Matteo T., Markoff S., Richstone D. O., 2009, ApJ, 706, 404
Heisler C. A., De Robertis M. M., 1999, AJ, 118, 2038
Hildebrand R. H., 1983, QJRAS, 24, 267
Ho L. C., Filippenko A. V., Sargent W. L., 1995, ApJS, 98, 477
Ho L. C., Filippenko A. V., Sargent W. L., 1997, ApJS, 112, 31
Ho L. C., Greene J. E., Filippenko A. V., Sargent W. L., 2009, ApJS, 183, 1
Ivanov V. D., Rieke G. H., Groppi C. E., Alonso-Herrero A., Rieke M. J., Engelbracht C. W., 2000, ApJ, 545, 190
Kang W.-R., Woo J-H., Schulze J., Riechers D. A., Kim S. C., Park D., Smolcic V., 2013, ApJ, 767, 26
Kennicutt R. C., 1998, ARA&A, 36, 189
Kennicutt R. C., Evans N. J., 2012, ARA&A, 50, 531
Kormendy J. Bender R., Cornell M. E., 2011, Nature, 469, 374
Kormendy J., Ho L. C., 2013, ARA&A, 51, 511
Kormendy J., Kennicutt R., 2004, ARA&A, 42, 603
Kotilainen J. K., Hyvönen T., Reunanen J., Ivanov V. D., 2012, MNRAS, 425, 1057
Kuntschner H., 2000, MNRAS, 315, 184
Maraston C., 2005, MNRAS, 362, 799
Marleau F. R. et al., 2006, ApJ, 646, 929
Márquez I. Masegosa J., Durret F., González Delgado R. M., Moles M., Maza J., Pérez E., Roth M., 2003, A&A, 409, 459
Martins L. P., Rodríguez-Ardila A., Diniz S., Gruenwald R., de Souza R., 2013a, MNRAS, 431, 1823
Moorwood A. F. M., Oliva E., 1988, A&A, 203, 278
Naab T. et al., 2013, MNRAS, 444, 3357
Nemmen R., Bower R., Babul A., Storchi-Bergmann T., 2007, MNRAS, 377, 1652
Origlia L., Moorwood A. F. M., Oliva E., 1993, A&A, 280, 5360
Rayner J. T., Cushing M. C., Vacca W. D., 2009, ApJS, 185, 289
Riffel R. A., 2010, Ap&SS, 327, 239
Riffel R., Rodríguez-Ardila A., Pastoriza M. G., 2006, A&A, 457, 61
Riffel R., Pastoriza M. G., Rodríguez-Ardila A., Maraston C., 2007, ApJ, 659, L103
Riffel R. A., Storchi-Bergmann T., Winge C., McGregor P. J., Beck T., Schmitt H., 2008, MNRAS, 385, 1129
Riffel R. A., Storchi-Bergmann T., Riffel R., Pastoriza M. G., 2010, ApJ, 713, 469
Riffel R., Riffel R. A., Ferrari F., Storchi-Bergmann T., 2011, MNRAS, 416, 493
Rothberg B., Fischer J., 2010, ApJ, 712, 318
Rothberg B., Fischer J., Rodrigues M., Sanders D. B., 2013, ApJ, 767, 72
Sánchez-Blázquez P. et al., 2006, MNRAS, 371, 703
Sauvage M. et al., 2010, A&A, 518, 64
Silge J. D., Gebhardt K., 2003, ApJ, 125, 2809
Silva D. R., Kuntschner H., Lyubenova M., 2008, ApJ, 674, 194
Springel V., Di Matteo T., Hernquist L., 2005, ApJ, 620, 79
Storchi-Bergmann T., Riffel R. A., Riffel R., Diniz M. R., Borges Vale T., McGregor P. J., 2012, ApJ, 755, 87
Terlevich R., Davies R. L., Faber S. M., Burstein D., 1981, MNRAS, 196, 381
Thuan T. X., Sauvage M., 1992, A&AS, 92, 749
Valluri M., Merritt D., Emsellem E., 2004, ApJ, 602, 66
van der Marel R. P., Franx M., 1993, ApJ, 407, 525
Vanderbeke J., Baes M., Romanowsky A. J., Schimidtobreick L., 2011, MNRAS, 412, 2017
Weingartner J. C., Draine B. T., 2001, ApJ, 548, 296
Winge C., Riffel R. A., Storchi-Bergmann T., 2009, ApJS, 185, 186
Xiao T., Barth A. J., Greene J. E., Ho L. C., Bentz M. C., Ludwig R. R., Jiang Y., 2011, ApJ, 739, 28

APPENDIX A: FITS OF THE SPECTRA

Figs A1 and A2 show the resulting fit of the galaxy spectra for the CO and Ca triplet spectral regions, respectively.

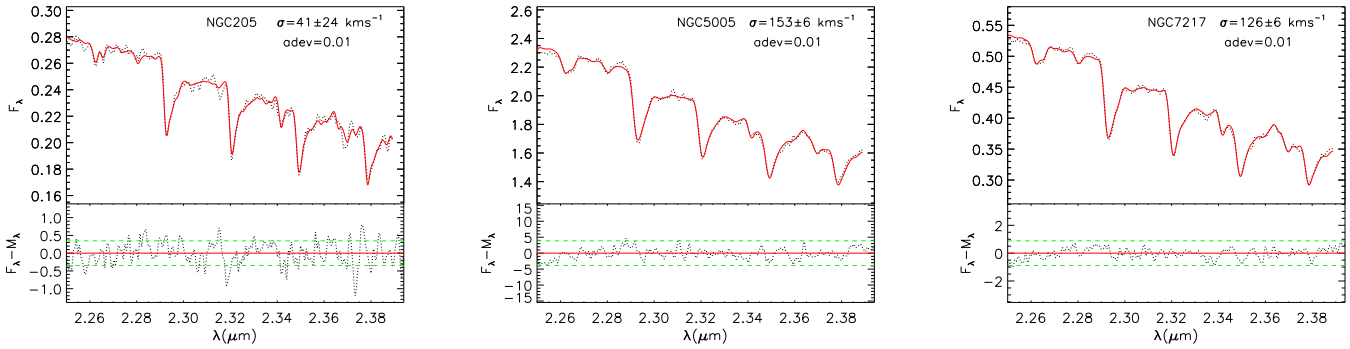

Figure A1. Sample fits of the CO absorptions band heads. The observed spectra are shown as dotted lines and the best-fitting model as continuous lines. In the bottom panels, the residuals of the fits (observed model) are shown as dotted lines, where the dashed lines show the 1σ level of the continuum. Fluxes are shown in units of 10^{-15} erg s^{-1} cm^{-2} Å $^{-1}$ and the residuals in units of 10^{-17} erg s^{-1} cm^{-2} Å $^{-1}$. The *adev* parameter shown at each panel gives the percentage mean $|OM|/O$ deviation over all fitted pixels, where O is the observed spectrum and M is the model. The fits for all spectra are available online only.

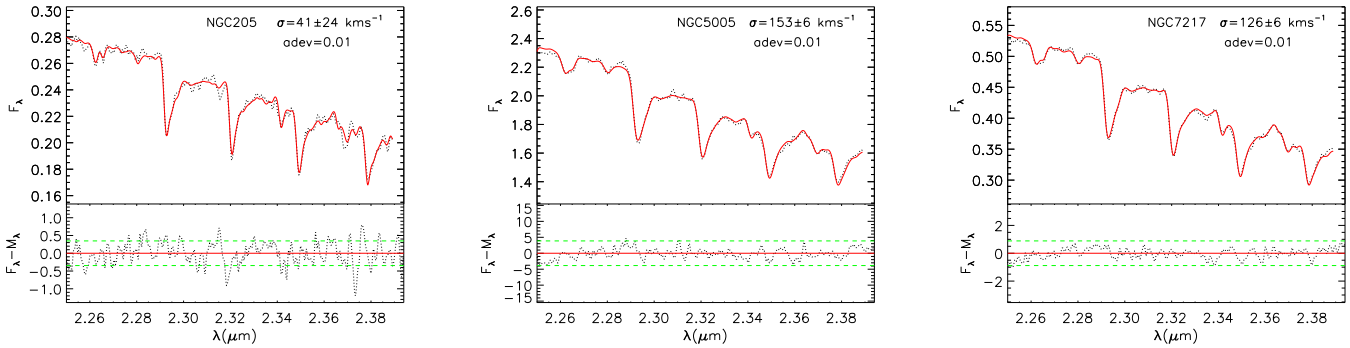

Figure A2. Same as Fig. A1 for the Ca triplet.

APPENDIX B: STELLAR TEMPLATES USED TO FIT THE STELLAR KINEMATICS

Table B1 shows the weights of each star (as well their spectral types) to the fit of the galaxy spectra for the CaT and CO spectral regions.

Table B1. Sample of the stellar templates used for each galaxy to derive the stellar kinematics. Column 1: galaxy name; columns 2–4: spectral and luminosity class, name and percentage contribution of the star to the fit of the galaxy spectrum for the Ca triplet region. Templates are from Cenarro et al. (2001) and for some cluster stars, the authors list the positions of the stars in the HR diagram (SGB: subgiant branch; GB: giant branch and HB: horizontal branch). Columns 5–7: same as columns 2–4 for the CO spectral region. Templates are from Winge et al. (2009). The full table is available online only.

	CaT region			CO region		
Galaxy	Spectral type	Star	Weight (per cent)	Spectral type	Star	Weight (per cent)
NGC 1358	HB	M71-1-34	44	M2III	HD30354	57
	HB	M71-C	9	M2	BD+59 274	7
	K4III	HD149161	6	K8V	HD113538	33
	M5III	HD172816	24	M0III	HD2490	1
	M7III	HD114961	15			
NGC 1961	GB	NGC 188-I-57	27	M2III	HD30354	36
	K0V	HD149661	9	K8V	HD113538	24
	K5III	HD139669	39	M0III	HD2490	39
	M5.5III	HD94705	19			
	M6V	BD+19-5116-B	2			
	M7III	HD114961	1			
NGC 2273	HB	M5-II-53	8	M2III	HD30354	18
	K4II	HD130705	39	K3Iab	HD339034	1
	K5III	HD139669	1	K8V	HD113538	1
	M4III	HD17491	20	M0III	HD2490	19
	M5III	HD172816	8	K0IV	HD34642	4
	M5.5III	HD94705	1	G5II	HD36079	33
	M5III	HD175865	7	K7III	HD63425B	3
	SGB	M67-F-115	10	G8V	HD64606	11
	SGB	M67-F-125	5	G3V	HD6461	6
NGC 2655	F3III	HD115604	6	M2III	HD30354	7
	GB	M67-F-108	7	K3Iab	HD339034	1
	HB	M5-II-53	8	K8V	HD113538	25
	K5III	HD139669	31	M0III	HD2490	40
	M6III	HD18191	22	K0IV	HD34642	1
	SGB	M67-F-125	24	K7III	HD63425B	23
NGC 2768	GB	NGC 188-I-85	8	M2III	HD30354	23
	HB	M71-1-41	16	K3Iab	HD339034	1
	HB	M92-XII-24	4	K8V	HD113538	19
	K3III	HD102328	37	K1II	HD198700	3
	M6III	HD18191	24	M0III	HD2490	49
	SGB	M67-F-125	7	K0IV	HD34642	2
NGC 2832	F0	BD-01-2582	1			1
	HB	M71-C	41	M2III	HD30354	30
	HB	M92-XII-24	2	K8V	HD113538	17
	M5.5III	HD94705	20	M0III	HD2490	51
	M6V	BD+19-5116-B	16			
	M7III	HD207076	6			
	SGB	M67-F-125	10			
NGC 3031	GB	M67-F-231	1	M3III	HD27796	5
	GB	M92-XII-8	2	M2III	HD30354	14
	GB	NGC 188-II-122	6	K8V	HD113538	21
	HB	M5-II-76	1	M0III	HD2490	10
	HB	M92-I-13	3	K0IV	HD34642	2
	K5III	HD139669	5	G5II	HD36079	8
	M5III	HD172816	25	K7III	HD63425B	25
	M7III	HD114961	18	G3V	HD6461	10
	SGB	M67-F-115	7	K4III	HD9138	1
	SGB	M67-IV-68	29			

SUPPORTING INFORMATION

Additional Supporting Information may be found in the online version of this article:

Appendix A: Fits of the spectra.
Appendix B: Stellar templates used to fit the stellar kinematics.
(http://mnras.oxfordjournals.org/lookup/suppl/doi:10.1093/mnras/stu2256/-/DC1).

Please note: Oxford University Press are not responsible for the content or functionality of any supporting materials supplied by the authors. Any queries (other than missing material) should be directed to the corresponding author for the paper.

[1]*Departamento de Física/CCNE, Universidade Federal de Santa Maria, 97105-900, Santa Maria, RS, Brazil*
[2]*Kavli Institute for Astronomy and Astrophysics, Peking University, Beijing 100871, China*
[3]*Department of Astronomy, School of Physics, Peking University, Beijing 100871, China*
[4]*Gemini Observatory, Northern Operations Center, 670 N. Aohoku Place, Hilo, HI 96720, USA*
[5]*Laboratório Nacional de Astrofísica/MCT, Rua dos Estados Unidos 154, Itajubá, MG, Brazil*
[6]*NAT – Universidade Cruzeiro do Sul, Rua Galvão Bueno, 868, São Paulo 01506-000, SP, Brazil*
[7]*Instituto de Física, Universidade Federal do Rio Grande do Sul, CP 15051, Porto Alegre 91501-970, RS, Brazil*
[8]*Gemini Observatory, Southern Operations Center, Casilla 603, La Serena, Chile*
[9]*Astrophysics Department, Center for Astrobiology (CSIC-INTA), Torrejon de Ardoz, E-28850 Madrid, Spain*
[10]*Instituto de Fisica de Cantabria, CSIC-UC, E-39005 Santander, Spain*
[11]*Department of Physics, University of the Pacific, 3601 Pacific Avenue, Stockton, CA 95211, USA*
[12]*Instituto de Astrofísica de Canarias, Calle Vía Láctea, s/n, E-38205 La Laguna, Tenerife, Spain*
[13]*Departamento de Astrofísica, Universidad de La Laguna, E-38205 La Laguna, Tenerife, Spain*
[14]*Centro de Radioastronoma y Astrofsica (UNAM), Apartado Postal 3-72 (Xangari), 58089 Morelia, Mexico*
[15]*Departamento de Astronomía, Universidad de Chile, Casilla 36-D, Santiago, Chile*
[16]*Department of Physics and Astronomy, Macquarie University, NSW 2109, Australia*
[17]*Astrophysics Research Institute, Liverpool John Moores University, IC2, Liverpool Science Park 146 Brownlow Hill, Liverpool L3 5RF, UK*
[18]*Department of Physics & Astronomy, University of Victoria, PO Box 1700, STN CSC Victoria, BC V8W 2Y2, Canada*
[19]*Department of Physics and Space Sciences, Florida Institute of Technology, 150 West University Boulevard, Melbourne, FL 32901, USA*

This paper has been typeset from a TEX/LATEX file prepared by the author.